JGR | Machine Learning and Computation

RESEARCH ARTICLE
10.1029/2026JH001416

A Machine-Learning Surrogate for Differentiable Phase Equilibrium Modeling of Mantle Rocks on a Planetary Scale

Philip Hartmeier[1] and **Pierre Lanari**[1]

[1]Institute of Earth Sciences, University of Lausanne, Lausanne, Switzerland

Abstract Modeling processes within Earth's and other planetary bodies' mantle requires constraints from phase equilibrium to infer how changes in phase abundance and composition affect physical properties and geochemical processes. When applying such thermodynamic models on a planetary scale, performance becomes especially crucial. We present a fast and scalable machine-learning surrogate that can approximate phase equilibrium predictions for mantle rocks. The model was calibrated on a large synthetic data set ($n = 2.0{\cdot}10^6$) generated using a Gibbs free energy minimizer. This data set covers upper- to transition-zone mantle conditions in terms of pressure, temperature, and typical bulk rock composition. Evaluation of the model indicates uncertainties of less than ±0.01 molmol^{-1} for the prediction of phase fractions and less than ±0.005 molmol^{-1} for compositional variables within solid solutions. Gradient-based analysis identifies phase transitions that are sensitive to bulk chemistry changes. Peridotite fertility exerts a secondary, yet locally decisive, control on the seismic discontinuities and buoyancy contrasts that influence mantle convection. The assessment of computational performance indicates a speed up of four orders of magnitude when emulating phase equilibrium predictions with the GPU accelerated surrogate.

Plain Language Summary Predicting which minerals form the rocks of Earth's and other planets mantles and how their compositions vary with pressure and temperature is fundamental for understanding processes in planetary interiors. However, physics-based models, so-called free energy minimizers, are computationally expensive, limiting their use in very large-scale models. We developed a machine-learning model that rapidly approximates the precise predictions of such free energy minimizers. This model is trained on data that covers a wide range of possible rock compositions. Our approach can approximate the predictions with a high accuracy and precision. The variables that control the stability of minerals can be found by calculating derivatives across the model. The machine-learning model is up to 10′000 times faster than the fastest free energy minimizer. This improvement makes it feasible to incorporate predictions on the presence and composition of minerals into large-scale simulations of planetary mantles.

Key Points:

- A neural-network surrogate can approximate phase equilibrium predictions with a precision of <±0.01 molmol^{-1} for compositional variables
- The surrogate lowers computational time to <100 ns per point, two to four orders of magnitudes faster compared to Gibbs energy minimization
- Providing ultra-fast, precise and fully differentiable phase equilibrium predictions for large-scale thermo-mechanical and inversion codes

Supporting Information:

Supporting Information may be found in the online version of this article.

Correspondence to:

P. Hartmeier,
philip.hartmeier@unil.ch

Citation:

Hartmeier, P., & Lanari, P. (2026). A Machine-learning surrogate for differentiable phase equilibrium modeling of mantle rocks on a planetary scale. *Journal of Geophysical Research: Machine Learning and Computation*, *3*, e2026JH001416. https://doi.org/10.1029/2026JH001416

Received 19 APR 2026
Accepted 17 AUG 2026

Author Contributions:

Conceptualization: Philip Hartmeier, Pierre Lanari
Formal analysis: Philip Hartmeier
Funding acquisition: Pierre Lanari
Investigation: Philip Hartmeier
Methodology: Philip Hartmeier
Software: Philip Hartmeier
Supervision: Pierre Lanari
Writing – original draft: Philip Hartmeier
Writing – review & editing: Pierre Lanari

1. Introduction

Phase transitions and mineral reactions are both the result of and a driver for endogenic processes such as convection or melting within the geosphere of planetary bodies. Therefore, understanding phase equilibrium is crucial for observing the resulting geophysical signature and modeling such processes. These processes are inherently linked to planetary formation, evolution, and ultimately the potential development of a habitable biosphere (Jakosky & Byrne, 2025). Tellurian planets are characterized by a mantle and crust dominated by silicate minerals rich in Mg and Fe (Plesa et al., 2026). Many of these minerals form continuous solutions between their magnesian and ferrous endmembers, with additional minor components dissolved within their structures. At depths of the mantle transition zone between 410- and 660-km a series of phase transitions can occur that have drastic effects on the physical rock properties (Katsura & Ito, 1989). On Earth, with its active plate tectonic system, the upper to transition zone mantle is of particular interest as this is where most evidence of subducting slabs can be found (Fukao & Obayashi, 2013), mantle derived magmatism originates (Green & Ringwood, 1967), and potentially large quantities of water could be stored (Huang et al., 2005; Pearson et al., 2014). The presence and extent of these processes on other tellurian planets is a subject of active research (Dong et al., 2022).

Equilibrium thermodynamics allows petrological phase equilibrium to be modeled when combined with free energy minimizers, which can perform energy minimization calculations of complex, multi-component silicate solid solutions (e.g., Connolly & Kerrick, 1987; de Capitani & Brown, 1987; Riel et al., 2022; Stixrude & Lithgow-Bertelloni, 2005, 2011). These minimizers can predict the stable phase assemblage, phase fractions and

compositions, and other thermodynamic state variables, for example, heat capacity or compressibility of the system at equilibrium for a given pressure, temperature and bulk composition. They require a thermodynamic framework with equations of state and a thermodynamic database containing a set of experimentally determined thermodynamic properties. The minimizers have been successfully employed for thermobarometry and the simulation of rock-forming processes in petrology (Lanari & Duesterhoeft, 2019), to provide physical constraints to large-scale geodynamic models (Nakagawa et al., 2010), couple thermo-mechanical processes to chemical reactions in reactive transport models (Riel et al., 2018) and invert the chemical properties and mineralogical composition of Earth's and other planetary mantle from geophysical observation (Khan & Connolly, 2008).

When coupling increasingly larger, up to planetary-scale, thermo-mechanical models with phase equilibrium predictions, performance becomes ever more crucial. This in turn renders computationally costly methods such as free energy minimization no longer efficient and results in the use of precalculated lookup tables for a limited set of bulk compositions (Rummel et al., 2020; Zunino et al., 2011). Recent progress in machine-learning (ML), in particular in the field of physics-informed neural networks, has shown great potential in the very fast approximation of complex physical solvers using ML surrogates (Karniadakis et al., 2021). Such methods have been successfully applied within other geoscientific disciplines, for example, climate modeling (Rasp et al., 2018), pore-scale reactive transport (Prasianakis et al., 2020) and the inversion of ionospheric properties (Gross & Cohen, 2020). Within earth sciences and geophysics, ML models have been successfully calibrated for the fast prediction of seismic properties of peridotite (Kerswell et al., 2024), melt composition (Candioti et al., 2025), or thermal evolution of planetary mantles (Agarwal et al., 2020). Besides providing fast approximations, ML surrogates are also inherently differentiable functions. This enables gradient-based optimization methods for solving complex inversion problems where the forward model is itself a non-differentiable simulator (e.g., Shirobokov et al., 2020).

In this study, a ML surrogate is used to predict the stable phase fractions ($\boldsymbol{v}$) and compositions ($\boldsymbol{X}$) from pressure (P)–temperature (T) and bulk rock composition ($\boldsymbol{x}_{\text{bulk}}$) of mantle rocks. Such a prediction of state variables of individual phases poses particularly challenging, compared to the prediction of thermo-mechanical state variables of the bulk system (e.g., density and seismic wave velocities, Kerswell et al., 2024), as for each prediction only a subset from a large collection of potentially stable phases form the equilibrium assemblage and have defined properties. To our knowledge, previous studies predicting phase specific properties have focused on a limited number of phases besides bulk properties (melt composition, Candioti et al., 2025; aqueous speciation, Prasianakis et al., 2020). To address these limitations, we present a combined classifier–regressor architecture using a pretrained phase stability prediction. The surrogate is calibrated on a training data set generated with MAGEMin (Riel et al., 2022) using the thermodynamic database of Stixrude and Lithgow-Bertelloni (2022), covering a wide range of P–T conditions and possible variability in $\boldsymbol{x}_{\text{bulk}}$. In the following sections, the model is benchmarked against MAGEMin in accuracy, precision and computational performance. Finally, a gradient-based analysis is used to identify phase transitions that are sensitive to P, T or compositional changes.

2. Methods and Data

A neural network was calibrated as a surrogate model $\hat{f}$ to learn a mapping from P–T and $\boldsymbol{x}_{\text{bulk}}$ to $\boldsymbol{v}$ and $\boldsymbol{X}$ of stable phases:

$$\hat{f} : (P, T, \boldsymbol{x}_{\text{bulk}}) \mapsto (\boldsymbol{v}, \boldsymbol{X}), \tag{1}$$

where P and T are positive scalars and $\boldsymbol{x}_{\text{bulk}}$ is a six-component compositional vector of SiO_2–CaO–Al_2O_3–FeO–MgO–Na_2O. The predicted $\boldsymbol{v}$ and $\boldsymbol{X}$ are a 20-component vector of the potentially stable phases and a 6×20 matrix of the oxide components in these phases. So formally the problem poses a mapping:

$$\hat{f} : \mathbb{R}^{1+1+6} \mapsto \mathbb{R}^{20+6\times20} \tag{2}$$

The petrological justification of the chosen dimensionality of the problem space is provided in Section 2.1. All $\boldsymbol{v}_i$ and $\boldsymbol{X}_{j,i}$ of a phase i that is not predicted to be stable must be zero. Further, all compositional variables $\boldsymbol{x}_{\text{bulk}}$, $\boldsymbol{v}$ and the column vectors in $\boldsymbol{X}$ are not fully independent of each other and must satisfy a closure constraint when

summing over their respective components. This means that the components x_i of $\boldsymbol{v}$ and the column vectors in $\boldsymbol{X}$ must sum to one.

$$\sum_i x_i = 1 \tag{3}$$

And the predicted $\boldsymbol{v}$ and $\boldsymbol{X}$ must respect mass-balance with respect to the input $\boldsymbol{x}_{\text{bulk}}$ so that

$$\boldsymbol{X}\boldsymbol{v}^{\top} = \boldsymbol{x}_{\text{bulk}} \tag{4}$$

holds true.

2.1. Model Architecture and Calibration

A fully connected neural network is calibrated as the machine-learning surrogate. Each layer evaluates an input vector or a matrix of an input batch $\boldsymbol{x}$ to the respective output $\boldsymbol{y}$ by an affine transformation using the weight matrix $\boldsymbol{W}$ and the bias vector $\boldsymbol{b}$, followed by a non-linear activation σ:

$$\boldsymbol{y} = \sigma(\boldsymbol{W}\boldsymbol{x} + \boldsymbol{b}) \tag{5}$$

A rectified linear unit (ReLU) is used as an activation function. The implementation and training are done using the Julia programming language (Bezanson et al., 2017) relying on the machine-learning library Flux.jl and Zygote.jl for automatic differentiation (Innes, 2018).

Compositional variables in pure phases, for example, SiO_2 in quartz, and fixed components in solid solutions, for example, SiO_2 in olivine, are trivial and do not need to be predicted. Instead $\boldsymbol{X}$ is divided into a constant 6×6 $\boldsymbol{X}_{\mathbf{pp}}$ and a predicted 6×14 $\boldsymbol{X}_{\mathbf{ss}}$. The fixed components in $\boldsymbol{X}_{\mathbf{ss}}$ are injected into the prediction with a Hadamard product by

$$\boldsymbol{X}'_{\mathbf{ss}} = \boldsymbol{X}_{\mathbf{ss}} \odot \boldsymbol{M} + \boldsymbol{F} \tag{6}$$

where $\boldsymbol{M}$ is a Boolean matrix of whether the component i,j in $\boldsymbol{X}_{\mathbf{ss}}$ is fixed and $\boldsymbol{F}$ is the components value.

As the set of potentially stable phases is much larger than the phases that make up a stable assemblage, any prediction of phase fractions and compositions will be dominated by variables of phases that are not stable and their respective entries in $\boldsymbol{v}$ and $\boldsymbol{X}_{ss}$ are therefore equal to zero. This problem characteristic is taken care of in the model architecture by passing the input, or a learned embedding of it, to two heads within the model. A first head uses a sigmoid activation in its output to predict a vector $\boldsymbol{p}$ of 20 phase wise binary classification probabilities of whether the phase $\boldsymbol{p}_i$ is part of the stable assemblage. This output is combined by elementwise multiplication with the second head's prediction of $\boldsymbol{v}$ and $\boldsymbol{X}_{\mathbf{ss}}$, multiplying $\boldsymbol{p}$ elementwise with the row vectors, to bring all variables of not stable phases directly close to zero.

$$\boldsymbol{X}'_{\mathbf{ss}} = \boldsymbol{X}_{\mathbf{ss}} \odot \boldsymbol{p} \tag{7}$$

$$\boldsymbol{v}' = \boldsymbol{v} \odot \boldsymbol{p} \tag{8}$$

This classification head of the surrogate can be pretrained or learned simultaneously. Details on the model calibration and hyperparameter tuning are provided in the Supporting Information S1.

For the calibration of $\hat{f}$ a quadratic misfit $\mathcal{L}_2$ is minimized.

$$\mathcal{L}_2 : (|\hat{\boldsymbol{v}} - \boldsymbol{v}|)^2 + \left(\left|\hat{\boldsymbol{X}}_{\text{ss}} - \boldsymbol{X}_{\text{ss}}\right|\right)^2 \tag{9}$$

This misfit is expanded by a penalty for deviations from the closure condition (Equation 3), that is, column vector $\boldsymbol{x}$ of $\boldsymbol{v}$ and $\boldsymbol{X}_{\text{ss}}$ that do not sum to 0 or 1.

$$\mathcal{L}_c : \left(s^2 * (1-s)^2\right)^{\alpha}, \text{where } s = \sum_i x_i \text{ and } \alpha = 1 \tag{10}$$

Additionally, any violation of the mass-balance (Equation 4) is penalized by:

$$\mathcal{L}_m : \left|\boldsymbol{x}_{\text{bulk}} - \boldsymbol{X}\boldsymbol{v}^{\top}\right| \tag{11}$$

The final loss $\mathcal{L}$ that is optimized during the model calibration is obtained by summing Equations 9–11 and summed over a batch of data. For the pre-training of the classifier head, a binary cross-entropy loss is used.

Besides the loss $\mathcal{L}$ additional metrics are used to monitor convergence during training. The pretraining of the classifier head predicting $\boldsymbol{p}$ is monitored using an assemblage quality-factor (Q_{asm}), the fraction of incorrectly predicted phases and the fraction of assemblages with at least one incorrectly predicted phase. The Q_{asm} misfit after Duesterhoeft and Lanari (2020), is the complement of the Jaccard index between the predicted and true assemblages:

$$Q_{\text{asm}} = 1 - \frac{\sum_i \hat{p}_i \wedge p_i}{\sum_i \hat{p}_i \vee p_i} \tag{12}$$

Besides relying on $\mathcal{L}$ and its individual constituents, the evaluation of the complete surrogate relies on the mean absolute deviation (MAE) for $\boldsymbol{v}$ and $\boldsymbol{X}_{\mathbf{ss}}$ and the mean relative absolute deviation (MRE) respectively. For both MAE and MRE it is assumed that the prediction of zeros is relatively trivial. Therefore, these metrics are evaluated only considering the true positive and false negative predicted stable phases, optionally including the false positives as well, to obtain a robust conservative metric. Further methodological details regarding hyperparameter tuning can be found in the Supporting Information S1.

2.2. Model Sensitivity Analysis

As a neural network approximates the phase equilibrium predictions by a differentiable function, fast and quantitative derivative-based sensitivity analysis is possible using automatic-differentiation with Zygote.jl (v.0.7.10, Innes, 2018). The sensitivity with respect to an input S_i is calculated as norm of the Jacobian-vector product between the Jacobian $\boldsymbol{J}_{\hat{f}}$ of the surrogate $\hat{f}$ and an input vector $\boldsymbol{v}_i$.

$$S_i = \left\|\boldsymbol{J}_{\hat{f}}\boldsymbol{v}_i\right\|_2 \tag{13}$$

Whereas v_i can be a vector $\hat{\mathrm{e}}_i$ from the standard basis of the input vector space or a specific direction within that vector space, for example, the direction of mantle depletion and enrichment.

$$\boldsymbol{v}_{\text{BAS}-\text{HRZ}} = \begin{bmatrix} 0_2 \\ x_{\text{BAS}} - x_{\text{HRZ}} \end{bmatrix} \left\| \begin{bmatrix} 0_2 \\ x_{\text{BAS}} - x_{\text{HRZ}} \end{bmatrix} \right\|_2^{-1} \tag{14}$$

Where x_{BAS} and x_{HRZ} are constant six-component vectors of the compositions of basalt and harzburgite after Xu et al. (2008). To consider the scale difference for different input variables all $\mathbf{v}_i$ are scaled to represent a step equivalent to the unit vector in temperature $\hat{e}_T$, that is, 1 K. For a single output of interest, for example, stability, mode or a single compositional variable of phase k, the directional derivative $\nabla_{\boldsymbol{v}_i}\hat{f}_k$ can be calculated from the gradient $\nabla\hat{f}_k$ and $\boldsymbol{v}_i$.

$$\nabla_{\boldsymbol{v}_i}\hat{f}_k = \nabla^{\top}\hat{f}_k\boldsymbol{v}_i \tag{15}$$

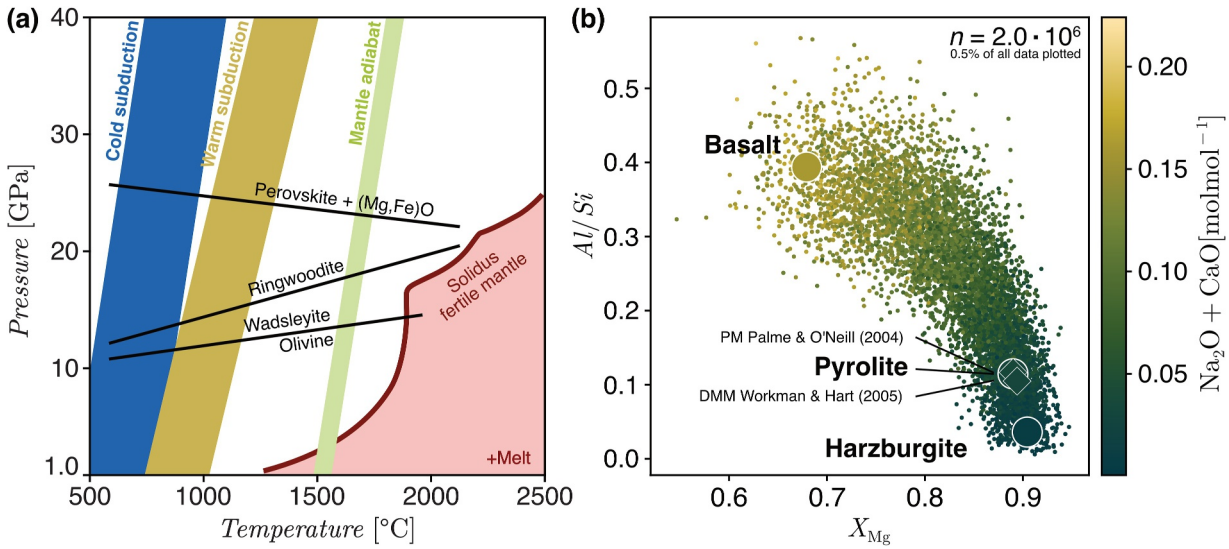

Figure 1. Domain of the training data used for the calibration of the ML surrogate. (a) Pressure and temperature are sampled uniformly within conditions covering the upper and transition-zone mantles, reaching into the lower mantle. Phase transitions for the $(Mg,Fe)_2SiO_4$-polymorphs were calculated using MAGEMin for the pyrolytic bulk from Xu et al. (2008). The lower limit of the temperature distribution is given by subduction geotherms (warm: Ganguly et al., 2009; cold: Thompson, 1992). The upper limit was guided by the temperature of the peridotite solidus (Zerr et al., 1998). The average mantle adiabat is taken from (Katsura et al., 2010). (b) Compositional variability covered by the training data. Points are randomly sampled from a Dirichlet distribution along the mixing line between harzburgite and basalt (composition from Xu et al., 2008). Geochemical bulk mantle estimates from Palme and O'Neill (2004) and Workman and Hart (2005) are shown as a comparison.

This directional derivative then quantifies the response of an output variable to an infinitesimal step in the direction of $\boldsymbol{v}_i$.

2.3. Training Data Set: Defining the P–T–x_{bulk} Space

MAGEMin (v1.8.5, Riel et al., 2022) was used to generate data for the model calibration. The conditions within the Earth's mantle were sampled for P within a range of 1–40 GPa, covering mantle depths from the MOHO beyond the 660-km seismic discontinuity (Dziewonski & Anderson, 1981), and T within a range 500–2500°C (Figure 1a), covering conditions from cold slabs (Thompson, 1992) to the fertile peridotite solidus (Takahashi, 1986; Zerr et al., 1998). Both P and T are sampled from uniform distributions within these bounds. The determination of a suitable distribution to describe the heterogeneity of mantle rock $\boldsymbol{x}_{\text{bulk}}$ is more challenging. Following (Stixrude & Lithgow-Bertelloni, 2022), the components SiO_2–CaO–Al_2O_3–FeO–MgO–Na_2O were chosen. These are the oxides of the most abundant non-volatile elements in the sun (Lodders, 2003) and together make up >98 wt% of geochemical estimates for the bulk silicate mantle (Palme & O'Neill, 2004; Workman & Hart, 2005). Sampling such a high-dimensional space completely would be highly inefficient. A better approach is to define a suitable subspace with geochemical relevance. The complex chemical heterogeneity of the mantle can be simplified to the $\boldsymbol{x}_{\text{bulk}}$-variability that is resulting from partially melting a pyrolytic reservoir into a basaltic melt and a harzburgitic residue; and the consequential re-mixing of these lithologies via subduction of lithospheric plates into the mantle (Stixrude & Lithgow-Bertelloni, 2012; Xu et al., 2008). Thus, mean $\bar{\boldsymbol{x}}_{\text{bulk}}$ vectors are sampled along the mixing line between a basalt (x_{BAS}) and harzburgite (x_{HRZ}) composition (Figure 1b), defined by:

$$\bar{\boldsymbol{x}}_{\text{bulk}} = f_{\text{BAS}} x_{\text{BAS}} + \left(1 - f_{\text{BAS}}\right) x_{\text{HRZ}} \tag{16}$$

with the basalt fraction f_{BAS} ranging from zero to one. To add some random noise to the input distribution and expand the subspace considered for the model calibration, $\boldsymbol{x}_{\text{bulk}}$ is then drawn form a Dirichlet distribution:

$$\boldsymbol{x}_{\text{bulk}} \sim \text{Dirichlet}(\boldsymbol{\alpha}), \text{where } \boldsymbol{\alpha} = \lambda \bar{\boldsymbol{x}}_{\text{bulk}} \tag{17}$$

The concentration parameter $\boldsymbol{\alpha}$ is obtained by scaling $\overline{\boldsymbol{x}}_{\text{bulk}}$ by the scalar λ. Using this parametrization each $\boldsymbol{x}_{\text{bulk}}$ samples compositions with an expectation $\overline{\boldsymbol{x}}_{\text{bulk}}$ and, by setting $\lambda = 100$, a 1-σ uncertainty per oxide corresponding to the equivalent of ±10 mol% in SiO_2. A total of 2'000'000 triplets of P–T–$\boldsymbol{x}_{\text{bulk}}$ were sampled from the corresponding distributions and the corresponding equilibrium state variables for $\boldsymbol{\nu}$ and $\boldsymbol{X}$ are predicted with MAGEMin using the thermodynamic data set of Stixrude and Lithgow-Bertelloni (2022). For the P–T–$\boldsymbol{x}_{\text{bulk}}$ conditions considered, corundum and post-perovskite are never predicted to be stable. This reduces the set of potentially stable phases to quartz (qtz), coesite (coe), stishovite (st), kyanite (ky), nepheline (neph), Ca-perovskite (capv), plagioclase (pl), spinel (sp), olivine (ol), wadsleyite (wa), ringwoodite (ri), orthopyroxene (opx), clinopyroxene (cpx), "high-pressure clinopyroxene" (hpcpx), akimotoite (ak), garnet-majorite (gtmj), perovskite (pv), Ca-ferrite (cf), magnesiowüstite (mw) and the "new aluminous phase" (nal). Additionally, a validation and test data set each containing 100′000 points was generated by sampling the same distributions.

3. Results and Discussion

3.1. Model Accuracy and Precision

The evaluation of the ML surrogate on the test data ($n = 10^5$) shows that the predicted phase assemblage, fraction and composition can match the Gibbs energy minimization (GEM) to a great level of detail. The expected uncertainty in surrogate predictions is given by errors in the order of 10^{-2} molmol^{-1} or less for the compositional variables $\boldsymbol{\nu}$ and $\boldsymbol{X}_{\text{ss}}$. Each group of variables is discussed separately in the following paragraphs.

Predicted assemblages show a quality-factor misfit (Equation 12) of 3.7%. Phase-wise resolved examination indicates that the stability for all phases is generally predicted with an accuracy of >95%, recalling >99% of the truly stable phases except for nepheline (82%) and kyanite (87%) (Figure 2). Notable is the comparably lower accuracy for Ca-perovskite and stishovite. These phases show a slight tendency for false positive predictions, which can be explained by their high but preferential abundance in Ca- and Si-rich, that is, more basaltic, $\boldsymbol{x}_{\text{bulk}}$ resulting in a pronounced imbalance in the training data. The relatively lower recall of the extremely rarely occurring nepheline and kyanite can be explained by this mechanism as well. In the following, only the true positive and false negative cases, that is, a phase is stable in the ground-truth, have been considered for both the uncertainties in predicted $\boldsymbol{\nu}$ and $\boldsymbol{X}_{\text{ss}}$. The good performance of the classifier head has the effect that correctly predicting the properties of a not stable phase to be zero is becoming trivial. The reported uncertainties are therefore conservative estimates. By assessing different performance metrics for stishovite and Ca-perovskite with significant false positives, it has been confirmed that the uncertainty estimates are indeed smaller if false positive cases are also considered.

The errors associated with the prediction of $\boldsymbol{\nu}$ are mostly within ±0.01 molmol^{-1}, corresponding to a relative deviation of less than ±5% for most phases (Figure 2c). Notable exceptions are the pronounced and systematic underestimation of plagioclase abundance and the generally large relative errors associated with stability of the rare phases coesite, kyanite, nepheline and plagioclase. The relatively rare and low abundance phases show increased relative errors of ±10% for high-pressure clinopyroxene and akimotoite and 20% for spinel.

The errors associated with the prediction of $\boldsymbol{X}_{\text{ss}}$ are mostly within ±0.005 molmol^{-1}, corresponding to a relative deviation well below ±5% for most phases (Figures 3a and 3b). The only exception to this is plagioclase, which exhibits relatively higher absolute and relative errors. The small error in both $\boldsymbol{\nu}$ and $\boldsymbol{X}_{\text{ss}}$ result in minuscule deviation from mass-balance for all six components with respect to $\boldsymbol{x}_{\text{bulk}}$ (Figure 3c). For the example of garnet, a solid solution incorporating all six chemical components, we illustrate the element-wise error analysis (Figure 3d), which can be found fully in the Supporting Information S1.

3.1.1. Discussion of the Model Accuracy and Precision

The predicted mineral assemblages are reproduced with both high accuracy and recall, and the error distributions for most compositional variables are closely centered around zero, showing only minor systematic deviations. The surrogate is therefore capable of accurately matching GEM-based phase equilibrium predictions. A notable exception is equilibria involving plagioclase, where the model systematically underestimates the phase fraction of plagioclase. As plagioclase plays an important role in both mechanical properties (Birch, 1961) and geochemical processes (e.g., partial melting Green & Ringwood, 1967) in the uppermost mantle, this is a relevant limitation for

10.1029/2026JH001416

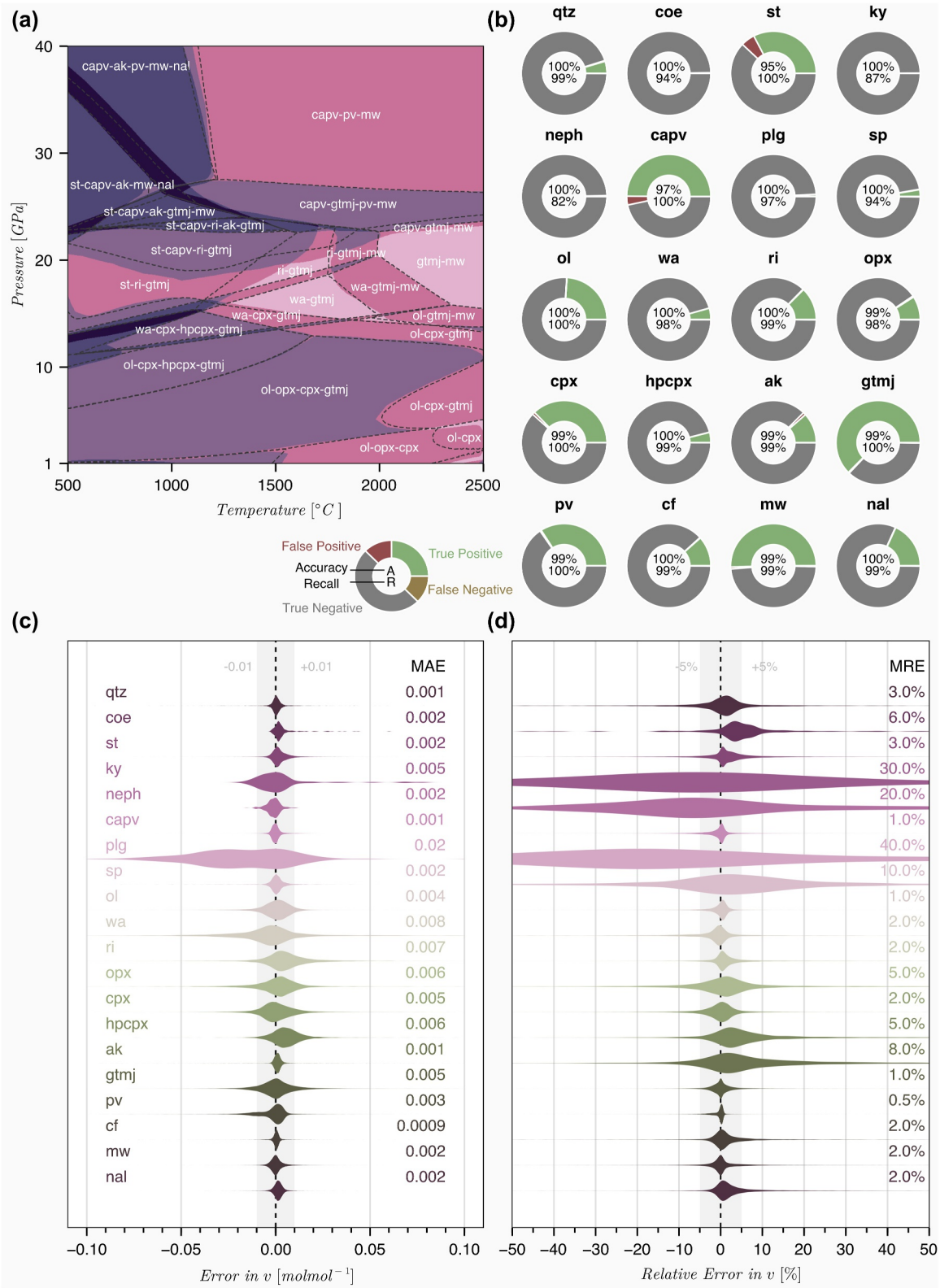

Figure 2.

applications focusing on the uppermost 30 km of the mantle. For such applications we strongly advise refining the calibration with a data set sampling the relevant P–T–$\boldsymbol{x}_{\text{bulk}}$ conditions in more details.

The phase fractions of plagioclase, kyanite, nepheline, and, to a lesser degree, spinel show a distribution of relative errors with long tails (Figure 2b). All of these are low-abundance phases that are only stable under a narrowly restricted set of P–T–$\boldsymbol{x}_{\text{bulk}}$ conditions (see Figure S2 in the Supporting Information S1). For the composition of solid solutions, akimotoite shows a long positive tail in the relative error distribution, which can be linked to high relative errors associated with very low values of MgO and FeO in akimotoite for conditions where an Al-rich akimotoite is predicted to be stable instead (Figure S7 in the Supporting Information S1). Similarly, the long negative tail for magnesiowüstite can be linked to predicted small dissolved quantities of α-$NaAlO_2$. These high relative errors are therefore interpreted to primarily reflect dividing by small values of the associated target variable, and, except for plagioclase, are not associated with high absolute deviations. Consequently, the high relative errors tend to correlate with the zero-mode lines associated with the phase transitions that produce or consume these phases. If any of these phases are of particular interest, the applicability of the surrogate presented here will require careful consideration and potential fine-tuning, for example, by explicitly oversampling or weighting the loss for these phases.

The remaining random errors associated with the surrogate predictions must be contextualized with uncertainties associated with GEM-based phase equilibrium modeling. For a successful minimization, the deviation in Gibbs free energy of the individual solid solutions relative to the stable hyperplane must be $<10^{-6}$ J (Riel et al., 2022). Hence, the uncertainties arising from the GEM itself are very low. Therefore, the uncertainty of a phase equilibrium prediction will be dominated by the uncertainty of the thermodynamic database (Lanari & Duesterhoeft, 2019). The propagation of errors associated with thermodynamic parameters and activity–composition models into phase equilibrium modeling remains an area that has been vastly under-explored. This precludes the possibility of a systematic comparison. Recent calibrations of thermodynamic data report uncertainties for compositional variables of up to ±0.3 site fractions (Weller et al., 2024). Depending on the site multiplicity, speciation and number of total sites in a phase, this converts to different uncertainties when expressed as a mol fraction of a component. For example, considering Mg on the three-fold M1 site in the garnet model of this database, this would correspond to a maximal molar uncertainty of $\sim\pm0.13$ molmol^{-1}. In conclusion, while the precision of a GEM-prediction will be order of magnitudes more precise than the surrogate's precision, the deviations are most likely within the relevant uncertainties stemming from the original calibration of thermodynamic parameters used in the GEM.

3.1.2. Application Outside the Training Data Set

The surrogate was used to predict $\boldsymbol{\nu}$ and $\boldsymbol{X}_{\text{ss}}$ for the $\boldsymbol{x}_{\text{bulk}}$ of an altered oceanic crust (Kelley et al., 2003) under mantle conditions. These predictions are compared to a ground-truth from GEM. The results of that comparison imply that even when applied outside the original training data space and therefore forced to go beyond mere interpolation, the model can predict phase equilibrium reasonably well. Mineral stability is predicted with >90% accuracy and compositional variables of commonly occurring phases are predicted with an error of <0.05 molmol^{-1} for $\boldsymbol{\nu}$ and <0.03 molmol^{-1} for $\boldsymbol{X}_{\text{ss}}$. While we would still advise against the application of the surrogate outside of the training data space without prior tuning on domain specific data, these results show a high generalization capability. This is interpreted as evidence that the surrogate converged to a mapping which at least partially is close to thermodynamic state functions that are generally true.

Figure 2. Uncertainties in the prediction of mineral assemblage and mineral fraction ν. (a) Mineral assemblage diagram predicted with the classifier of the ML surrogate for a pyrolytic bulk composition (Xu et al., 2008). Surrogate predictions, with a resolution of $10{,}00^2$, are shown as fields shaded by their variance. For readability only the assemblages of large fields are labeled. Assemblage boundaries predicted with MAGEMin are shown as black stippled lines for comparison. (b) Pie diagrams of phase-wise phase stability classification on the test data set ($n = 10^5$) showcasing the fraction of predictions that are truly stable (green), truly absent (gray), falsely stable (red) and falsely absent (yellow). The phase-wise classification accuracy and recall are reported in percentage. (c) Distribution of phase-wise absolute and (d) relative error in ν. For each phase, the median absolute and relative absolute errors are given as uncertainty estimates. Note that relative errors are inflated for variables with small true values.

10.1029/2026JH001416

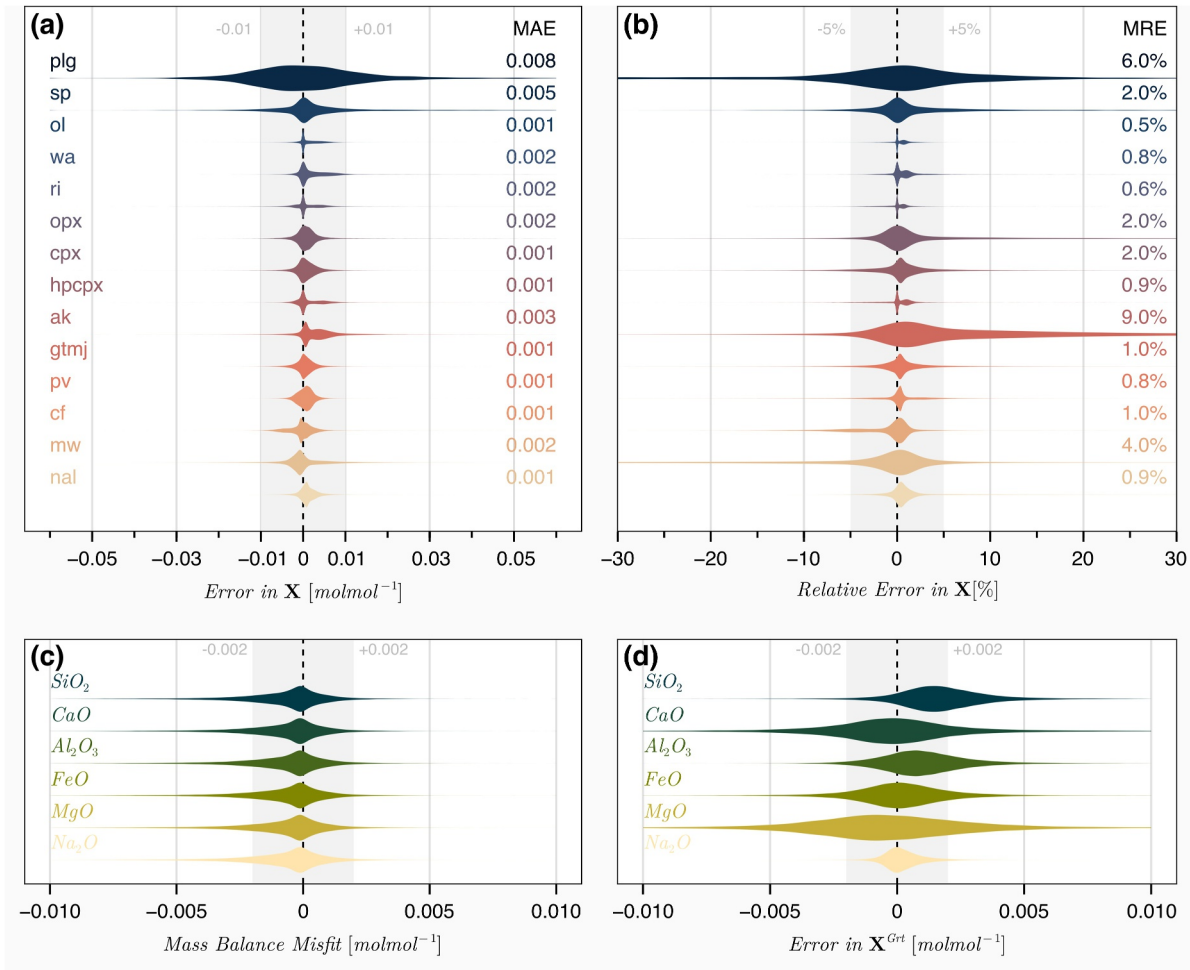

Figure 3. Uncertainties in the prediction of solid-solution composition $\boldsymbol{X}_{\mathrm{ss}}$ and mass-balance on the test data set ($n = 10^5$). (a) Distribution of phase-wise absolute and (b) relative error in $\boldsymbol{X}_{\mathrm{ss}}$. For each phase, the median absolute and relative absolute errors are given as uncertainty estimates. Note that relative errors are inflated for variables with small true values. (c) Element-wise deviations from mass-balance between the input $\boldsymbol{x}_{\mathrm{bulk}}$ and the product of $\boldsymbol{\nu}$ and $\boldsymbol{X}$. The small deviations confirm that there is only insignificant mass loss induced by the surrogate predictions. (d) Element-wise resolved errors for $\boldsymbol{X}_{\mathrm{ss}}^{\mathrm{grt}}$. These detailed metrics can be found for all phases in the Supporting Information S1.

3.2. Controls on Mantle Assemblages and Geodynamic Implications

The trained surrogate enables a quantitative sensitivity analysis of phase equilibrium predictions with respect to all input variables simultaneously. Here, this gradient-based analysis (Equations 13 and 15) is applied to the mineral assemblage diagram for a pyrolytic bulk composition (Figure 2) to inspect the physical and chemical control on the predicted phase assemblage (Figures 4 and 5). The Jacobian of the surrogate, that is, the matrix of all partial derivatives for each prediction with respect to the model input, quantifies how strongly each model output responds to each input. Multiplying the Jacobian by a vector representing a specific direction in the input space, for example, an increase in T or a step along $\boldsymbol{\nu}_{\mathrm{BAS-HRZ}}$ (Equation 14), yields a vector of directional derivatives, one value per output, quantifying its response to an infinitesimal step in that direction (Equation 15). Physically, evaluating $\boldsymbol{\nu}_{\mathrm{BAS-HRZ}}$ quantifies bulk compositional changes toward more enriched or depleted mantle compositions. The norm of this Jacobian–vector product is taken as the overall sensitivity of the model predictions to a given input direction (Equation 13).

Mineral assemblages are most sensitive to changing P and T and only to a second order controlled by compositional changes when plotted in P–T space (Figure 4). The excellent agreement between the high sensitivity to P, barometers, or T, thermometers, with the Clapeyron slope $\frac{\mathrm{dP}}{\mathrm{dT}}$ of the respective reactions is interpreted as proof that this method can correctly identify controlling variables. Changes in the bulk rock composition, along a depleted-

10.1029/2026JH001416

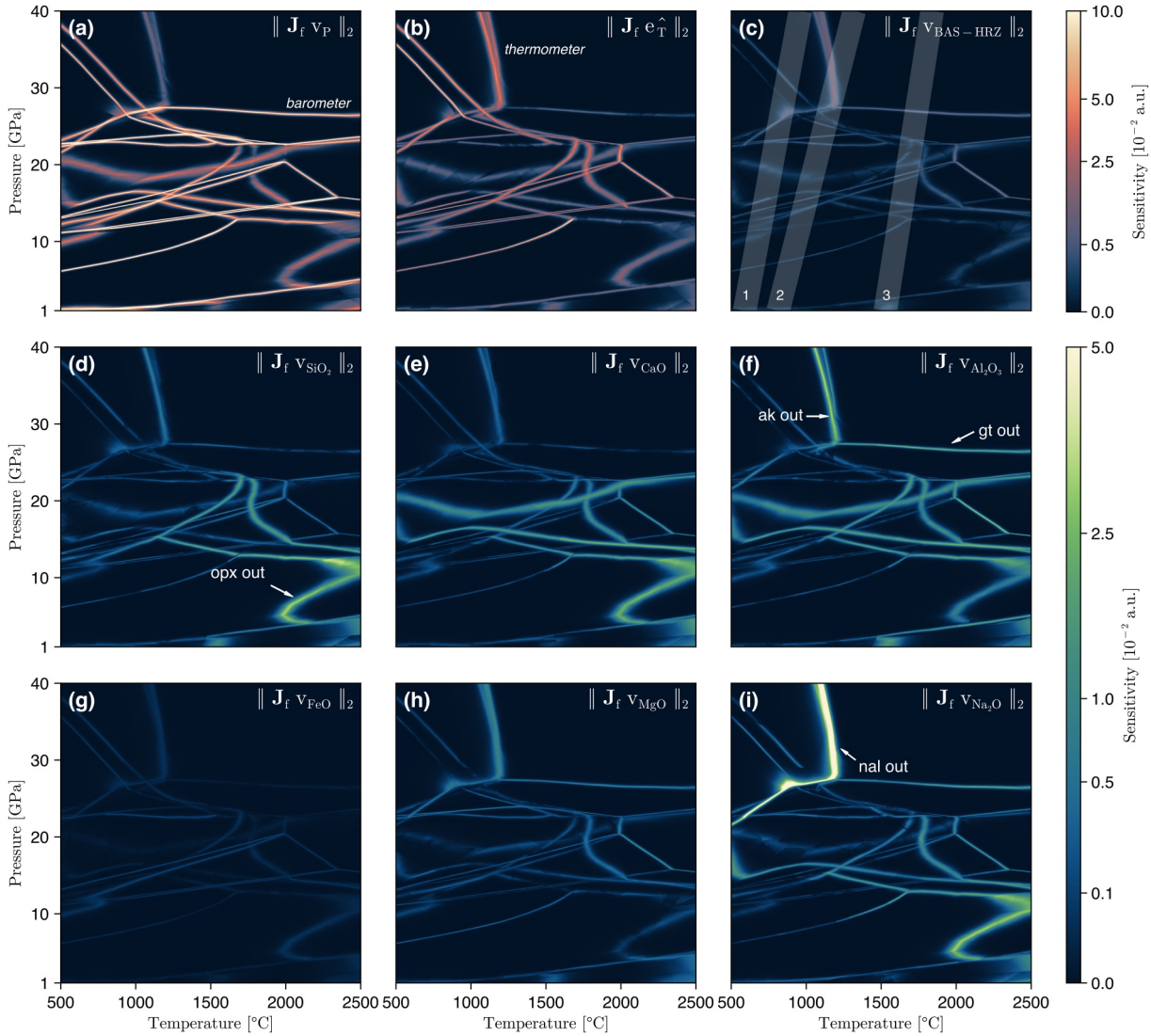

Figure 4. Sensitivity of the predicted mineral assemblage topology for a pyrolytic bulk composition across *P–T* space with respect to (a) pressure, (b) temperature, (c) mantle fertility, (d) SiO_2-, (e) CaO-, (f) Al_2O_3-, (g) FeO-, (h) MgO-, and (i) Na_2O-contents. The vectors $\boldsymbol{\nu}_i$ are scaled to represent a step equivalent to 1 K in temperature. Gray areas in panel (c) show typical geotherms for cold (1, Thompson, 1992) and warm subduction (2, Ganguly et al., 2009) and a mantle adiabat (3, Katsura et al., 2010). Note that the color-scale is non-linear to accompany the large differences in magnitude.

to-enriched direction of mantle fertility, most strongly affect reactions above 25 GPa or 2000°C (Figure 4c). A comparison with the mineral assemblage diagram (Figure 2) shows that composition-sensitive phase transitions involve the stability of the "new aluminous phase", akimotoite and garnet-majorite. The dissociation of (Mg, Fe)$_2SiO_4$-polymorphs to garnet-majorite and magnesiowüstite toward ultra-high *T*, >2000°C, is likely rarely attained within Earth's present-day mantle as they lie significantly above the mantle adiabat, and therefore not further discussed here.

For the "new aluminous phase", changes in Na_2O, and to a lesser degree MgO, content assert the compositional control over its stability (Figures 4d–4i). The stability of akimotoite and garnet-majorite is most sensitive to the Al_2O_3 content on the other hand. Assemblage boundaries are generally less sensitive to CaO and SiO_2, with the most sensitive ones being the Opx-out toward high temperatures in the upper mantle (Figure 4d). As MgO and FeO are mostly involved in second-order phase transitions by exchange equilibria between ferromagnesian phases, phase boundaries in a mineral assemblage diagram are generally the least sensitive to changes in those components.

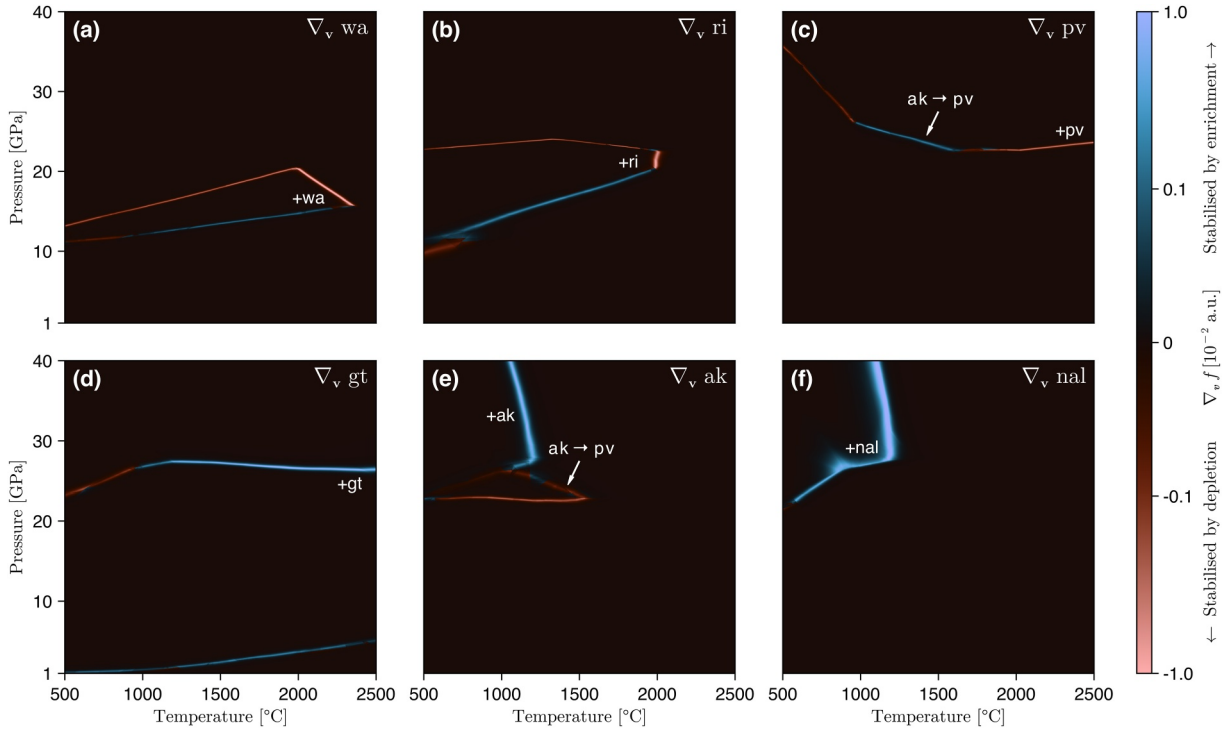

Figure 5. Directional derivatives of phase boundaries with respect to the compositional vector difference between Basalt and Harzburgite, that is, mantle fertility. Positive derivatives indicate expansion of a phase's stability toward more enriched bulk compositions, while negative derivatives indicate a stabilization toward more depleted bulk compositions. Differential stability is shown for (a) wadsleyite, (b) ringwoodite, (c) perovskite (bridgmanite), (d) garnet-majorite, (e) akimotoite, and (f) "new aluminous phase." Note that the color-scale is non-linear to accompany the large differences in magnitude.

Directional derivatives allow us to assess whether a change in mantle fertility translates into relative stabilization or consumption of the individual phases (Figure 5). Akimotoite, the "new aluminous phase", and garnet-majorite are stabilized by more fertile peridotite compositions above 25 GPa. In the transition zone, the stability of akimotoite and the $(Mg,Fe)_2SiO_4$ polymorphs is expanding and wadsleyite is stabilized at the expense of ringwoodite with increasing depletion of the bulk chemistry.

Our findings support the hypothesis of Mookherjee et al. (2012) that the stability of the "new aluminous phase" depends heavily on whole-rock chemistry and that the phase is stabilized by an increase in alkalis. In fact, we can show that this reaction represents the most sensitive chemometer across *P–T* space in a pyrolytic mantle. Most relevant for mantle convection dynamics and seismic signatures are phase transitions involving the $(Mg,Fe)_2SiO_4$ polymorphs that are associated with distinct seismic discontinuities at depths of 410, 520, and 660 km (Frost, 2008). The phase transition associated with the 410-km discontinuity is among the least sensitive reactions with respect to changes in mantle fertility (Figures 4 and 5). The 520-km discontinuity, associated with the continuous transition from wadsleyite to ringwoodite, is here shown to be relatively sensitive to changes in bulk chemistry, shifting it toward higher *P* with increasing depletion of the mantle peridotites (Figures 5a and 5b). The associated seismic discontinuity is particularly weak and often indistinguishable from signal-processing artifacts (Frazer & Park, 2024). The fact that the position of the wadsleyite–ringwoodite transition is susceptible to small changes in mantle fertility offers an explanation for the absence of a sharp 520-km discontinuity. Hence, heterogeneous mantle depletion complements a previously proposed mechanism relating chemical heterogeneities to 520-km visibility, namely the dampening by elevated garnet modes for mantle regions with a high basalt fraction (Frazer & Park, 2024). For the 660-km discontinuity, the perovskite-forming akimotoite-out reaction (arrow in Figure 5), is of particular interest. This phase transition has a steep negative Clapeyron slope and is crossed by subduction associated mantle geotherms (Ganguly et al., 2009; Thompson, 1992). A steep negative Clapeyron slope of a perovskite-forming reaction, the transition to the lower mantle, promotes positive buoyancy of anomalously cold material, preventing the penetration of downgoing slabs into the lower mantle (Fukao et al., 2009). The presence of akimotoite as an intermediate between ringwoodite and perovskite has been

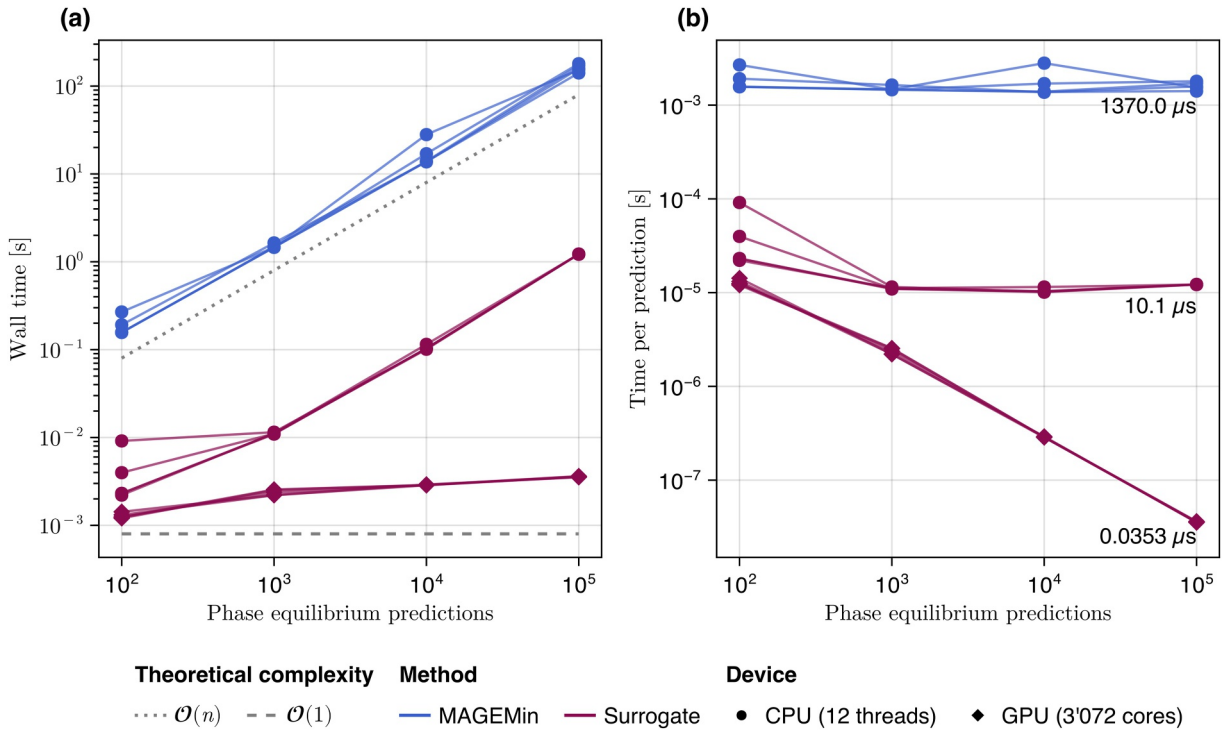

Figure 6. (a) Scaling comparison between Gibbs energy minimization with MAGEMin and the ML surrogate. Linear and constant time complexity are shown for comparison. (b) Computational time estimates normalized by the number of computed phase equilibrium predictions.

proposed to explain the observed ponding of slabs and associated depression of the seismic discontinuity beneath subduction zones (Cottaar & Deuss, 2016). Chanyshev et al. (2022) acknowledge the possibility of a compositional control over the akimotoite-to-perovskite reaction. We can demonstrate that for increasingly depleted mantle rocks, akimotoite stability near the 660-km discontinuity is favored at the expense of perovskite, potentially depressing the discontinuity. These findings highlight mantle fertility as a potential variable influencing buoyancy-changing phase transitions across the mantle transition zone, indicating a coupled thermochemical control of layered versus whole-mantle convection.

3.3. Computational Performance Comparison

Computational performance is crucial when phase equilibrium modeling is applied to large scale geodynamic models or used within inverse modeling methods. In such scenarios, the lesser precision but greater computational efficiency of a surrogate might be worth trading off against a GEM-based physical model, for example, MAGEMin. For this, the performance and scalability between the two approaches are compared. Both methods are benchmarked when predicting phase equilibrium for an increasingly larger set of points: 10^2, 10^3, 10^4 and 10^5. Each benchmark was performed on a machine with two Intel® Xeon® E5-2620v3 with 2×64 GB of RAM at the University of Lausanne, using single-precision floating-point arithmetic (float32). As the surrogate can take advantage of GPU acceleration, the surrogate benchmarks are repeated on an Nvidia® Geforce GTX TITAN X with 3072 Compute Unified Device Architecture (CUDA) cores and 12 GB GPU memory (GRAM). For each benchmark, a total of five trials are run. The data are loaded into RAM and GRAM beforehand, and a warm-up prediction is performed to exclude pre-compilation time.

The comparison indicates that an ML surrogate approximation of phase equilibrium is systematically two orders of magnitude faster than GEM (Figure 6). Surrogate predictions can be computed consistently as fast as 10 µs per point on the CPU. Both MAGEMin and the surrogate scale linearly with increasing number of predictions. However, when using GPU acceleration, the surrogate scales nearly constant with increasing number of predictions, accentuating the potential gains in computational speed. For large sets of predictions (10^5), the surrogate outperforms MAGEMin by over four orders of magnitude, resulting in a minimal prediction time per point of 35.3 ns. Importantly it must be noted that this comparison is only fair for scenarios where the lower precision of

the surrogate is acceptable and only $\boldsymbol{\nu}$ and $\boldsymbol{X}$ are of interest. MAGEMin would be capable of providing a plethora of additional thermodynamic variables, for example, mechanical moduli, heat capacities or entropy, at no increased computational cost.

These computational time requirements can be extrapolated to planetary scale mantle convection models (Nakagawa et al., 2010). Using the surrogate to predict the phase equilibrium for all the $2{\cdot}10^7$ tracers used in their model would require 0.7 s with the GPU performance estimate or 202 s with the CPU per time step.

4. Conclusion

We find that an ML surrogate can be calibrated to predict the compositional variables $\boldsymbol{\nu}$ and $\boldsymbol{X}_{\mathrm{ss}}$ from P–T–$\boldsymbol{x}_{\mathrm{bulk}}$ for phase equilibrium problems. The obtained calibration can predict these variables accurately and with a precision sufficient for petrological applications. The work presented in this contribution can be summarized by the following conclusions:

1. Following Xu et al. (2008), the complex chemical heterogeneity of Earth's mantle was reduced by simplifying the compositional variability to lie along a mixing line between basaltic and harzburgitic compositions. This allows for an effective sampling within the relevant problem domain, making it feasible to generate high-resolution training data.
2. The model architecture combining a mineral stability classification with a regression of compositional variables proved itself useful to tackle the difficulties of predicting properties which are phase specific and thus only defined when the corresponding phase is stable. In combination with the explicit consideration of first-order physical principles, that is, mass-balance and closure of compositional variables, in the misfit function, this allowed a surrogate model that can predict phase-specific thermodynamic variables to be calibrated, expanding the current capabilities of bulk properties emulation (Kerswell et al., 2024).
3. The evaluation on an independent test set has shown that the surrogate can match the physical model to a high degree of accuracy and precision. Assemblages, mineral modes and the composition of solid solutions can be predicted with errors that lie well within the requirements for practical applications and uncertainties stemming from the calibration of thermodynamic data used for GEM-based phase equilibrium modeling (Weller et al., 2024).
4. The close correspondence between computed sensitivities and known Clapeyron slopes, or the compositional components governing discontinuous and continuous phase transitions, validates the physical consistency of the surrogate. More significantly, the availability of analytic gradients with respect to all input variables opens a direct pathway to embedding gradients over phase equilibrium predictions within optimization-based inverse problems.
5. The evaluation of the computational performance has shown a stark decrease in computational time by multiple orders of magnitude. This, combined with the capability to compute predictions on a GPU, for which it could be shown that the computation scales very efficiently, and their inherent differentiability, make surrogates an extremely promising tool for heavy duty applications, for example, geodynamic solvers, inversions or reactive transport codes, requiring phase equilibrium predictions.

Our findings demonstrate that for applications where an increase in computational speed can be traded off against a reduced precision, to about $\Delta\boldsymbol{\nu} = \pm 0.01$ molmol^{-1} and $\boldsymbol{\Delta X}_{\mathrm{ss}} = \pm 0.005$ molmol^{-1}, ML surrogates show great potential to speed up GEM-based phase equilibrium models. Together with fast models predicting bulk properties (Kerswell et al., 2024), phase equilibrium can be coupled to large-scale geodynamic models. Predicted mineral modes and composition can be empirically linked to physical properties (Zhao et al., 2018) or used for equilibrium partitioning with trace components such as water in the mantle (Inoue et al., 2010). One particularly promising application is inversion problems, where gradients over a phase equilibrium prediction could greatly benefit the associated optimization problem.

Conflict of Interest

The authors declare no conflicts of interest relevant to this study.

Availability Statement

To reproduce the findings of this contribution, we provide an archived GitHub repository (Hartmeier, 2026) together with accompanying data sets (Hartmeier & Lanari, 2026).

Acknowledgments
We thank Andrin Rehmann for the inspiring discussion about scientific machine-learning that profoundly influenced the work in this contribution. Suzette Timmerman and Renée Tamblyn are thanked for their insights into defining a compositional space that adequately represents the chemical heterogeneities in the mantle and the relevance of such heterogeneities to mantle phase equilibria. We would like to thank Nicolas Riel, without MAGEMin this contribution would have not been possible. Editor Prof. Chen and two anonymous reviewers are thanked for their constructive comments and handling of the manuscript. This work was supported by the Swiss National Science Foundation (SNSF) under Grant 10007192. Generative AI has been used to improve the language and readability in the first version of the manuscript and for parts of the plotting related Julia scripts. Open access publishing facilitated by Universite de Lausanne, as part of the Wiley - Universite de Lausanne agreement via the Consortium Of Swiss Academic Libraries.

References

Agarwal, S., Tosi, N., Breuer, D., Padovan, S., Kessel, P., & Montavon, G. (2020). A machine-learning-based surrogate model of Mars' thermal evolution. *Geophysical Journal International*, *222*(3), 1656–1670. https://doi.org/10.1093/gji/ggaa234

Bezanson, J., Edelman, A., Karpinski, S., & Shah, V. B. (2017). Julia: A fresh approach to Numerical Computing. *SIAM Review*, *59*(1), 65–98. https://doi.org/10.1137/141000671

Birch, F. (1961). The velocity of compressional waves in rocks to 10 kilobars, part 2. *Journal of Geophysical Research: Special Issue - Elastic Properties and Equations of State*, *66*(7), 91–116. https://doi.org/10.1029/SP026p0091

Candioti, L. G., Nathwani, C., & Chelle-Michou, C. (2025). Validating thermodynamic models of arc-magma differentiation and training neural networks for rapid thermodynamic property inference. *ESS Open Archive*. https://doi.org/10.22541/essoar.176169621.16239367/v1

Chanyshev, A., Ishii, T., Bondar, D., Bhat, S., Kim, E. J., Farla, R., et al. (2022). Depressed 660-km discontinuity caused by akimotoite-bridgmanite transition. *Nature*, *601*(7891), 69–73. https://doi.org/10.1038/s41586-021-04157-z

Connolly, J., & Kerrick, D. (1987). An algorithm and computer program for calculating composition phase diagrams. *Calphad*, *11*(1), 1–55. https://doi.org/10.1016/0364-5916(87)90018-6

Cottaar, S., & Deuss, A. (2016). Large-scale mantle discontinuity topography beneath Europe: Signature of akimotoite in subducting slabs. *Journal of Geophysical Research: Solid Earth*, *121*(1), 279–292. https://doi.org/10.1002/2015jb012452

de Capitani, C., & Brown, T. H. (1987). The computation of chemical equilibrium in complex syste ms containing non-ideal solutions. *Geochimica et Cosmochimica Acta*, *51*(10), 2639–2652. https://doi.org/10.1016/0016-7037(87)90145-1

Dong, J., Fischer, R. A., Stixrude, L. P., Lithgow-Bertelloni, C. R., Eriksen, Z. T., & Brennan, M. C. (2022). Water storage capacity of the martian mantle through time. *Icarus*, *385*, 115113. https://doi.org/10.1016/j.icarus.2022.115113

Duesterhoeft, E., & Lanari, P. (2020). Iterative thermodynamic modelling—Part 1: A theoretical scoring technique and a computer program (Bingo-Antidote). *Journal of Metamorphic Geology*, *38*(5), 527–551. https://doi.org/10.1111/jmg.12538

Dziewonski, A. M., & Anderson, D. L. (1981). Preliminary reference Earth model. *Physics of the Earth and Planetary Interiors*, *25*(4), 297–356. https://doi.org/10.1016/0031-9201(81)90046-7

Frazer, W. D., & Park, J. (2024). No globally detectable seismic interfaces within Earth's mantle transition zone: Evidence for basalt enrichment. *Earth and Planetary Science Letters*, *641*, 118838. https://doi.org/10.1016/j.epsl.2024.118838

Frost, D. J. (2008). The upper mantle and transition Zone. *Elements*, *4*(3), 171–176. https://doi.org/10.2113/gselements.4.3.171

Fukao, Y., & Obayashi, M. (2013). Subducted slabs stagnant above, penetrating through, and trapped below the 660 km discontinuity. *Journal of Geophysical Research: Solid Earth*, *118*(11), 5920–5938. https://doi.org/10.1002/2013jb010466

Fukao, Y., Obayashi, M., & Nakakuki, T. (2009). Stagnant slab: A review. *Annual Review of Earth and Planetary Sciences*, *37*(1), 19–46. https://doi.org/10.1146/annurev.earth.36.031207.124224

Ganguly, J., Freed, A. M., & Saxena, S. K. (2009). Density profiles of oceanic slabs and surrounding mantle: Integrated thermodynamic and thermal modeling, and implications for the fate of slabs at the 660km discontinuity. *Physics of the Earth and Planetary Interiors*, *172*(3–4), 257–267. https://doi.org/10.1016/j.pepi.2008.10.005

Green, D. H., & Ringwood, A. E. (1967). The genesis of basaltic magmas. *Contributions to Mineralogy and Petrology*, *15*(2), 103–190. https://doi.org/10.1007/BF00372052

Gross, N. C., & Cohen, M. B. (2020). VLF remote sensing of the D Region ionosphere using neural networks. *Journal of Geophysical Research: Space Physics*, *125*(1), e2019JA027135. https://doi.org/10.1029/2019ja027135

Hartmeier, P. (2026). Philipsite/MantlePhaseEquilibriumSurrogate: V0.1.2. in (Version v0.1.2) [Software]. https://doi.org/10.5281/zenodo.18662170

Hartmeier, P., & Lanari, P. (2026). [Dataset]. *Accompanying data for "A machine-learning surrogate for Gibbs Free Energy minimization-based phase equilibrium modelling of mantle rocks on a planetary scale" (Hartmeier & Lanari, 2026) (Version v0.1.1)*. https://doi.org/10.5281/zenodo.18154881

Huang, X., Xu, Y. X., & Karato, S.-i. (2005). Water content in the transition zone from electrical conductivity of wadsleyite and ringwoodite. *Nature*, *434*(7034), 746–749. https://doi.org/10.1038/nature03426

Innes, M. (2018). Flux: Elegant machine learning with Julia. *Journal of Open Source Software*, *3*(25), 602. https://doi.org/10.21105/joss.00602

Inoue, T., Wada, T., Sasaki, R., & Yurimoto, H. (2010). Water partitioning in the Earth's mantle. *Physics of the Earth and Planetary Interiors*, *183*(1–2), 245–251. https://doi.org/10.1016/j.pepi.2010.08.003

Jakosky, B. M., & Byrne, P. K. (2025). Using Venus, Earth, and Mars to understand exoplanet Volatile and climate evolution. *Journal of Geophysical Research: Planets*, *130*(10), e2024JE008882. https://doi.org/10.1029/2024je008882

Karniadakis, G. E., Kevrekidis, I. G., Lu, L., Perdikaris, P., Wang, S., & Yang, L. (2021). Physics-informed machine learning. *Nature Reviews Physics*, *3*(6), 422–440. https://doi.org/10.1038/s42254-021-00314-5

Katsura, T., & Ito, E. (1989). The system Mg2SiO4-Fe2SiO4 at high pressures and temperatures: Precise determination of stabilities of olivine, modified spinel, and spinel. *Journal of Geophysical Research*, *94*(B11), 15663–15670. https://doi.org/10.1029/JB094iB11p15663

Katsura, T., Yoneda, A., Yamazaki, D., Yoshino, T., & Ito, E. (2010). Adiabatic temperature profile in the mantle. *Physics of the Earth and Planetary Interiors*, *183*(1–2), 212–218. https://doi.org/10.1016/j.pepi.2010.07.001

Kelley, K. A., Plank, T., Ludden, J., & Staudigel, H. (2003). Composition of altered oceanic crust at ODP Sites 801 and 1149. *Geochemistry, Geophysics, Geosystems*, *4*(6). https://doi.org/10.1029/2002gc000435

Kerswell, B., Cerpa, N. G., Tommasi, A., Godard, M., & Padrón-Navarta, J. A. (2024). RocMLMs: Predicting rock properties through machine learning models. *Journal of Geophysical Research: Machine Learning and Computation*, *1*(4), e2024JH000264. https://doi.org/10.1029/2024jh000264

Khan, A., & Connolly, J. A. D. (2008). Constraining the composition and thermal state of Mars from inversion of geophysical data. *Journal of Geophysical Research*, *113*(E7). https://doi.org/10.1029/2007je002996

Lanari, P., & Duesterhoeft, E. (2019). Modeling metamorphic rocks using equilibrium thermodynamics and internally consistent databases: Past achievements, problems and perspectives. *Journal of Petrology*, *60*(1), 19–56. https://doi.org/10.1093/petrology/egy105

Lodders, K. (2003). Solar System abundances and condensation temperatures of the elements. *The Astrophysical Journal*, *591*(2), 1220–1247. https://doi.org/10.1086/375492

Mookherjee, M., Karki, B. B., Stixrude, L., & Lithgow-Bertelloni, C. (2012). Energetics, equation of state, and elasticity of NAL phase: Potential host for alkali and aluminum in the lower mantle. *Geophysical Research Letters*, *39*(19). https://doi.org/10.1029/2012gl053682

Nakagawa, T., Tackley, P. J., Deschamps, F., & Connolly, J. A. D. (2010). The influence of MORB and harzburgite composition on thermo-chemical mantle convection in a 3-D spherical shell with self-consistently calculated mineral physics. *Earth and Planetary Science Letters*, *296*(3), 403–412. https://doi.org/10.1016/j.epsl.2010.05.026

Palme, H., & O'Neill, H. S. C. (2004). Cosmochemical estimates of Mantle composition. In H. D. Holland & K. K. Turekian (Eds.), *Treatise on geochemistry* (Vol. 2, pp. 1–38). Pergamon. https://doi.org/10.1016/B0-08-043751-6/02177-0

Pearson, D. G., Brenker, F. E., Nestola, F., McNeill, J., Nasdala, L., Hutchison, M. T., et al. (2014). Hydrous mantle transition zone indicated by ringwoodite included within diamond. *Nature*, *507*(7491), 221–224. https://doi.org/10.1038/nature13080

Plesa, A.-C., Maia, J., Adeli, S., & Rückriemen-Beza, T. (2026). Terrestrial planet surfaces and interiors. In D. Veras (Ed.), *Encyclopedia of astrophysics* (1st ed., pp. 19–37). Elsevier. https://doi.org/10.1016/B978-0-443-21439-4.00049-3

Prasianakis, N. I., Haller, R., Mahrous, M., Poonoosamy, J., Pfingsten, W., & Churakov, S. V. (2020). Neural network based process coupling and parameter upscaling in reactive transport simulations. *Geochimica et Cosmochimica Acta*, *291*, 126–143. https://doi.org/10.1016/j.gca.2020.07.019

Rasp, S., Pritchard, M. S., & Gentine, P. (2018). Deep learning to represent subgrid processes in climate models. *Proceedings of the National Academy of Sciences*, *115*(39), 9684–9689. https://doi.org/10.1073/pnas.1810286115

Riel, N., Bouilhol, P., van Hunen, J., Cornet, J., Magni, V., Grigorova, V., & Velic, M. (2018). Interaction between mantle-derived magma and lower arc crust: Quantitative reactive melt flow modelling using STyx. *Geological Society, London, Special Publications*, *478*(1), 65–87. https://doi.org/10.1144/sp478.6

Riel, N., Kaus, B. J. P., Green, E. C. R., & Berlie, N. (2022). MAGEMin, an efficient gibbs energy minimizer: Application to igneous systems. *Geochemistry, Geophysics, Geosystems*, *23*(7), e2022GC010427. https://doi.org/10.1029/2022gc010427

Rummel, L., Baumann, T. S., & Kaus, B. J. P. (2020). An autonomous petrological database for geodynamic simulations of magmatic systems. *Geophysical Journal International*, *223*(3), 1820–1836. https://doi.org/10.1093/gji/ggaa413

Shirobokov, S., Belavin, V., Kagan, M., Ustyuzhanin, A., & Baydin, A. G. (2020). Black-Box optimization with local generative surrogates. *Advances in Neural Information Processing Systems*.

Stixrude, L., & Lithgow-Bertelloni, C. (2005). Thermodynamics of mantle minerals - I. Physical properties. *Geophysical Journal International*, *162*(2), 610–632. https://doi.org/10.1111/j.1365-246X.2005.02642.x

Stixrude, L., & Lithgow-Bertelloni, C. (2011). Thermodynamics of mantle minerals - II. Phase equilibria. *Geophysical Journal International*, *184*(3), 1180–1213. https://doi.org/10.1111/j.1365-246X.2010.04890.x

Stixrude, L., & Lithgow-Bertelloni, C. (2012). Geophysics of chemical heterogeneity in the mantle. *Annual Review of Earth and Planetary Sciences*, *40*(1), 569–595. https://doi.org/10.1146/annurev.earth.36.031207.124244

Stixrude, L., & Lithgow-Bertelloni, C. (2022). Thermal expansivity, heat capacity and bulk modulus of the mantle. *Geophysical Journal International*, *228*(2), 1119–1149. https://doi.org/10.1093/gji/ggab394

Takahashi, E. (1986). Melting of a dry peridotite KLB-1 up to 14 GPa: Implications on the Origin of peridotitic upper mantle. *Journal of Geophysical Research*, *91*(B9), 9367–9382. https://doi.org/10.1029/JB091iB09p09367

Thompson, A. B. (1992). Water in the Earth's upper mantle. *Nature*, *358*(6384), 295–302. https://doi.org/10.1038/358295a0

Weller, O. M., Holland, T. J. B., Soderman, C. R., Green, E. C. R., Powell, R., Beard, C. D., & Riel, N. (2024). New thermodynamic models for anhydrous alkaline-silicate magmatic systems. *Journal of Petrology*, *65*(10), egae098. https://doi.org/10.1093/petrology/egae098

Workman, R. K., & Hart, S. R. (2005). Major and trace element composition of the depleted MORB mantle (DMM). *Earth and Planetary Science Letters*, *231*(1–2), 53–72. https://doi.org/10.1016/j.epsl.2004.12.005

Xu, W., Lithgow-Bertelloni, C., Stixrude, L., & Ritsema, J. (2008). The effect of bulk composition and temperature on mantle seismic structure. *Earth and Planetary Science Letters*, *275*(1–2), 70–79. https://doi.org/10.1016/j.epsl.2008.08.012

Zerr, A., Diegeler, A., & Boehler, R. (1998). Solidus of Earth's deep mantle. *Science*, *281*(5374), 243–246. https://doi.org/10.1126/science.281.5374.243

Zhao, Y.-H., Zimmerman, M. E., & Kohlstedt, D. L. (2018). Effect of iron content on the creep behavior of Olivine: 2. Hydrous conditions. *Physics of the Earth and Planetary Interiors*, *278*, 26–33. https://doi.org/10.1016/j.pepi.2017.12.002

Zunino, A., Connolly, J. A. D., & Khan, A. (2011). Precalculated phase equilibrium models for geophysical properties of the crust and mantle as a function of composition. *Geochemistry, Geophysics, Geosystems*, *12*(4). https://doi.org/10.1029/2010gc003304